Design and analysis of a composite beam for infrastructure applications

Part II: Preliminary investigation in shear and torsion

by

Mario Springolo[1], Gerard van Erp[2], Amar Khennane[3*]

[1,3] Faculty of Engineering and Surveying, The University of Southern Queensland, Toowoomba, Qld 4350, Australia

[2] Professor, Executive Director, Fibre Composite Design and Development Centre. The University of Southern Queensland, Toowoomba, Qld 4350, Australia

Abstract:

Bending behaviour was dealt with in the preceding prequel, its associated failure modes identified, and a simplified theoretical approach was proposed for design purposes. However, this approach would not be complete without a simplified method for estimating the shear resistance of the beam and its torsional response.

Keywords: composite beam, shear resistance, lateral torsion, moment-shear interaction, lateral buckling

*Lecturer, Faculty of Engineering and Surveying, The University of Southern Queensland, Toowoomba, Qld 4350, Australia
Tel: (+61) (7) 4631 1383, Fax: (+61) (7) 4631 2526, email: khennane@usq.edu.au

Biographical notes: Mr Mario Springolo received his PhD in February 2005 from the Faculty of Engineering and Surveying at USQ. He is currently working as a structural engineer with Larken Teys consulting Pty Ltd. http://www.larkinteys.com.au

Biographical notes: Professor Van Erp was born and educated in the Netherlands and moved to Asutralia in 1989. In 1990 he joined the Faculty of Engineering and Surveying at USQ. Currently, he is the Executive Director of Fibre Composites Design & Development, University of Southern Queensland (USQ) responsible of Australia's first fibre composites bridge.

Biographical notes: Dr Amar Khennane holds a BE from Tizi-Ouzou, Algeria, an M.Sc. from Heriot Watt, UK, and a PhD, from UQ, Australia. Before joining the Faculty of Engineering and Surveying at the University of Southern Queensland, he was a researcher with the Cooperative Research Centre for Advanced Composite Structures, Ltd, Australia. His research interests are in composite materials: micro-mechanics, durability and through life estimation of composite structures, and computational mechanics.

INTRODUCTION

FRP beams are known to experience high shear deformations [1,2,3,4,5,6], it is therefore necessary to include the effect of shear in describing their deformation under load. In addition, load eccentricities and/or geometrical imperfections, tend to cause a beam to twist towards its weaker axis. This lateral torsional buckling often precipitates bending failure. Consequently, it can become the primary failure mode of a beam. To avoid this scenario, lateral restraints are often provided. Determination of restraint locations is dependent upon the critical buckling load, which is a function of the un-restrained span, and the section properties of the beam.

In the following sections a simplified method will be developed to check the shear capacity of the proposed beam. However, since beams are rarely used in states of pure bending or pure shear, the interaction between the two loadings will also be investigated using the Timoshenko beam theory. A method for the determination of the torsion constant of the section is also proposed together with simple one-dimensional analysis to study the possibility of lateral torsional buckling.

PURE SHEAR

Shear – deformation behaviour

Like in the preceding prequel, the transformed section approach is also used to model shear behaviour. The shear modulus, *G*, is now used in conjunction with the widths of the lamina to produce the transformed section. The behaviour of the beam under shear loading is as shown on Figure 1.

The shear stiffness of the beam, *GA*, is initially that of the un-cracked section (region 1). The first cracks in the PFR appear at a loading of:

$$V_{cracked} = \frac{\tau_{f6} A_t}{1.785} \frac{G}{G_6} \tag{1}$$

where τ_{f6} is the failure shear stress of the core, A_t is the transformed area of the un-cracked section, G is the reference modulus of the transformed section, G_6 is the shear modulus of the core. The subscript 6 refers to the core material in Figure 1 of the preceding prequel. The derivation of equation (1) together with the coefficient of 1.785 were derived from a shear flow analysis of the section of the beam under consideration. The details of the complete derivation are given in [7].

Once cracking occurs, the beam becomes a hybrid of cracked and un-cracked sections. The beam continues to withstand further loading until failure of the web laminates (point 3). The behaviour of the beam and the progression of cracks are similar in nature to that discussed for pure bending in the preceding prequel. Using the same bilinear relationship adopted in the prequel, the effective shear stiffness for region 2 can be estimated as:

$$GA_{effective} = GA_{un-cracked} - \left(GA_{un-cracked} - GA_{cracked}\right) \frac{\left(V - V_{cracked}\right)}{\left(V_{ultimate} - V_{cracked}\right)} \tag{2}$$

where $V_{ultimate}$ is determined in the coming sections.

Assuming small deformation theory, the obtained effective stiffness can be used to estimate shear deformations as detailed in [7]

Shear stress distribution

As experimental tests revealed [7], shear behaviour of FRP materials is often characterised by yielding. In the opinion of the authors, failure may be therefore better defined through the use of a limiting stress criterion, which is best suited to characterise the onset of yielding.

The stress distribution throughout a beam undergoing shear loading is not uniform. The variation in stresses is characterised by the shear flow throughout the section, which can be estimated using the following equation [8]:

$$\tau_y = \frac{VQ_y}{It_y} \tag{3}$$

where: τ_y is the shear stress at the location a distance y from the neutral axis, V is the shear force acting on the beam, Q_y is the first moment of the area above y, to the neutral axis, I is the second moment of area of the section, and t_y is the width of the section at the distance y. By ignoring shear lag, the equation gives an average shear stress across the width of the section. Indeed, shear lag can be considered negligible for thin sections such as those used in FRP beam webs as reported in [8].

Using equation (3), two cases were modelled, respectively ignoring and allowing for the cracking of the core material. The obtained distributions are shown on Figure 2.

It can be seen that the shear stresses within the web laminates are much higher when cracking of the core is considered. In addition, it can be seen that the maximum shear stress value occurs in the webs for both cases. Hence, it is a common and reasonable practice to ignore flange contribution to shear resistance in box beams. However, for the sake of completeness, flange contributions are considered herein.

Calculation of the maximum shear stress is often facilitated by the introduction of a shear correction factor, k_3, to the average shear stress. This average shear stress is calculated by:

$$\tau_{ave} = \frac{V}{A_t} \tag{4}$$

The shear correction factor can be estimated by comparing the values obtained from equations (3) and (4). Figure 3 shows the variation of k_3 along the depth of the beam.

It appears from these values that the maximum shear stress in the webs can be calculated, using a shear flow analysis of the section [7], respectively for the un-cracked and cracked transformed sections as:

$$\tau_{un-cracked} = 1.785\frac{V}{A_t} \tag{5}$$

and:

$$\tau_{cracked} = 3.893\frac{V}{A_{t.c}} \tag{6}$$

where $A_{t.c}$ is the transformed area of the cracked section. Both the coefficients 1.785 and 3.893 derive from a shear flow analysis of the section of the beam under consideration. The details of the complete derivation are given in [7].

In equations (5) and (6) the transformed section is used to come up with a generic shear stress for the section. In reality, the shear stresses within the individual components of the web (lamina and PFR core) are different. Assuming strain compatibility, and using the modulus ratios for the transformed section and the particular laminate, they can be calculated as follows:

$$\tau_i = \frac{G_i}{G}\tau \tag{7}$$

where: τ_i and G_i are respectively the shear stress and shear modulus in laminate i, G is the reference modulus used for the transformed section, and τ is the shear stress calculated from equation (5) or (6). These stresses can then be compared with the capacities of the laminates to assess whether failure is likely to occur at the given shear loading.

Once the stresses in the beam have been determined, the failure modes can be defined with reference to these stresses.

SHEAR INDUCED FAILURE MODES

Cracking of the core

Excessive shear stresses in the beam can lead to a number of failure modes taking place. In particular, due to its brittle nature, cracking of the core material is likely to occur when the maximum shear stress in the web exceeds the failure shear stress of the PFR as shown in equation (1). It is expected that cracking will be initiated in the middle of the web where the shear stresses are the highest. Once the PFR is cracked, the web and flange laminates provide the only resistance to failure at crack locations, as they constitute the main shear reinforcement of the beam. With the addition of load, the cracks extend into the flanges causing a localised shear dislocation in the beam as shown on Figure 4. As a result, the inner RHS is no longer constrained by the core, and is prone to delaminating and buckling. Whereas the outer RHS laminate is still restrained and continues to resist the loading until it fails in a tensile mode.

Shear failure of the webs

Failure of the web is expected when the shear stress in the outer RHS laminate exceeds its shear capacity, which is determined as:

$$\tau_{f7} \leq 3.893 \frac{V}{A_{t.c}} \frac{G_7}{G} \tag{8}$$

where τ_{f7} is the shear capacity of the web laminate as determined using ISO 14129, which stipulate the testing of a coupon at $\pm 45^{o}$.

However, experimental results [7] reveal that the shear capacity of the web laminates is higher than that estimated using ISO 14129. It was also found that the shear strength of the web laminates is governed by fibre fracture. Therefore, equation (8) is reformulated to include fibre fracture [7] and results in:

$$3.893\frac{V}{A_{t.c}}\frac{G_7}{G} \geq \sigma_{f7}\phi_{f7}\cos 45 \tag{9}$$

Indeed, once the matrix cracks the fibres align themselves with the direction of the load as shown schematically on Figure 5. Equation 9 attempts to model the sequential failure behaviour of the laminate. It takes into account the residual load carrying ability of the fibres once the resin has failed.

The capacity of the fibres in tension has been determined by unidirectional tensile tests. By multiplying the cross sectional area of the specimen by the fibre fraction ratio (ϕ_f), the area of fibres in the unidirectional tests is found. The force at failure is then divided by the area of fibres to get the fibre fracture stress (σ_f) The fibres are orientated at 45 degrees in the webs, hence the cos45. So the RHS is the shear stress capacity and the LHS is the calculated shear stress.

Using the latest equation, a prediction of the ultimate shear capacity of the beam can be obtained as:

$$V_{ultimate} = \frac{A_{t.c}\sigma_{f7}\phi_{f7}G\cos 45}{3.893G_7} \tag{10}$$

Shear buckling of the webs

The thinner the web, the higher the likelihood that web buckling will precede shear failure. The principal stresses caused by shear are shown on Figure 6.

The compressive component of these principal stresses may cause buckling of the web. This type of buckling reduces the stiffness of the webs and leads to premature failure of the beam. Using a hinged boundary assumption, as adopted in the preceding prequel, a lower boundary solution for the critical shear buckling stress can be obtained [9]:

$$\sigma_{sb.cr} = \frac{5.35G\pi^2\left(t_w/d_b\right)^2}{12(1-\nu_w^2)} \tag{11}$$

where: the parameter 5.35 is based upon thin-walled plate theory for a plate with simply supported restraints, t_w is the thickness of the web, d_b is the depth of the void, and ν_w is the Poisson ratio of the web [7]. Comparison of the critical buckling and the maximum shear stresses within the web obtained respectively using equations (5) and (6) provides an indication as to when shear buckling of the web is likely to occur. It is apparent from equation (11) that the web thickness has a major affect upon capacity. A substantial rise in capacity can be achieved by a slight increase in web thickness.

Flange failure

While the webs resist the majority of the shear loading, the flange laminates also provide some resistance to shear. As a result, they are susceptible to undergo the following failure modes: shear failure of the laminates (L_1, L_2 or the core), and punching shear of the flange into the hollow core of the beam. Furthermore, the fibre orientation and geometry of the laminates do not provide any restraint against fibre pull-out, therefore the ISO 14129 recommended shear capacity applies.

Laminate failure in the flanges may happen when the shear stress exceeds the shear capacities of the outer laminates (L_1 or L_{14}), the unidirectional laminate (L_2 or L_{13}), and the core (L_3 or L_{12}); their respective failure criteria are given as:

$$\tau_{f1} \le \frac{V}{335.676 A_{t.c}} \frac{G_1}{G}, \tag{12}$$

$$\tau_{f2} \le \frac{V}{13.922 A_{t.c}} \frac{G_2}{G} \tag{13}$$

and

$$\tau_{f3} \le \frac{V}{2.138 A_t} \frac{G_3}{G} \tag{14}$$

where τ_{fi} is the failure shear stress of laminate i, and the coefficients in the denominators are obtained from the shear flow diagrams represented on Figure 3. In case of failure of the flanges, the shear force is entirely resisted by the webs. However, as the web carries most of the shear, this is unlikely since the shear loads required to cause flange laminate failures are well in excess of the webs shear capacity.

Punching shear of the flange into the beam hollow core may split the beam into two parts along the longitudinal axis. Such a catastrophic failure can happen if the shear stress within the flange exceeds the shear strength of the core in the flange:

$$\frac{V}{2.138 A_t} \frac{w_2 \sum_{i=1}^{4} G_i t_i}{4\left(\frac{\tau_{f3}}{\tau_{f1}}(t_1 + t_4) + t_2 + t_3\right)} \frac{1}{G} \ge \tau_{f3} \tag{15}$$

It is apparent from equation (15) that flange thickness can be increased with subsequent increase in capacity.

MOMENT – SHEAR INTERACTION

Deformation behaviour

The Timoshenko beam theory stipulates that the total deflection Δ_t of a beam under a combined loading of moment and shear can be decomposed into two additive components, namely flexural and shear:

$$\Delta_t = \Delta_m + \Delta_s \tag{16}$$

For a beam in four-point bending, where M is the moment and V is the shear force imposed on the beam. The values L and a are shown on Figure 7, the flexural and shear deflections are respectively given as:

$$\Delta_m = \frac{M\left(3La - 4a^2\right)}{6EI_{effective}} \tag{17}$$

and

$$\Delta_s = \frac{Va}{GA_{effective}} \tag{18}$$

Shear - moment capacity

Composite beams are known to experience a moment-shear interaction. That is the introduction of a moment into a beam affects its shear capacity and vice versa. Methods for predicting the moment-shear interaction for homogeneous beams exist in the literature [8,10,11, 2 , 3] namely: the linear relationship (Eurocomp), and the elliptical relationship.

Linear relationship (Eurocomp)

A linear relationship has been adopted by the Eurocomp design code [10]. It uses the following formula:

$$1 \geq \frac{V}{V_{u0}} + \frac{M}{M_{u0}} \tag{19}$$

for the determination of a moment-shear interaction diagram. Where V_{u0} and M_{u0} are respectively the ultimate capacities of the beam in pure shear and moment.

Elliptical relationship

When considering isotropic materials, the linear relationship mentioned above is conservative and is often replaced with an elliptical derivation that has its roots in the Mohr's circle method. For an isotropic material the general form is as follows:

$$1 \geq \left(\frac{V}{V_{u0}}\right)^2 + \left(\frac{N}{N_{u0}}\right)^2 \tag{20}$$

where N is the axial force applied. Given that the primary failure mechanism for the beams in flexure is one of an axial failure, the substitution of moment for axial force in equation (20) may be acceptable, therefore equation it becomes:

$$1 \geq \left(\frac{V}{V_{u0}}\right)^2 + \left(\frac{M}{M_{u0}}\right)^2 \tag{21}$$

This relationship is quadratic and allows higher combined loadings than the Eurocomp method. This method is also used for combined web buckling calculations [9]. A diagrammatic comparison between the models is given on Figure 8.

Proposed method

Through the use of the transformed section approach, it is possible to simulate the FRP beam as an isotropic medium. Cracking of the core will precipitate failure of the beam. Therefore, the cracked section is used in the analysis. The critical location depends on the ratio of moment to shear. However, unlike a real isotropic section, the angle the principal strain makes with the direction of the fibres in the laminates is of paramount importance. The most critical

situation happens when the first principal strain is normal to fibre direction. For each moment shear combination, the principal strains and their directions can be established, and compared with the material capacity to determine the critical location. By altering the magnitude of shear and moment loading, an interaction diagram can be produced. A detailed description of the method is given in [7].

Now that a number of models have been defined, they will be compared against FEA and experimental data in the next sequel to validate their applicability to FRP beam design.

LATERAL TORSIONAL RESISTANCE OF THE BEAM

Determination of the torsion constant

Torsion or twisting in a section induces shear stresses. In the case of a rectangular hollow section, such as the present FRP beam, the shear stresses induced within the flanges and webs will be of different magnitudes. The difference in magnitudes is due to the dissimilarity in the size, spatial location, and make-up of the flanges and webs. The core material could fail in tension from these shear stresses, and the section would continue to sustain further loads until ultimate failure. The mechanisms of pure shear discussed above are also applicable here. Distortional warping of the cross section is prevented by the applied boundary conditions used in the experimental set-up. As a result, there is no change in length of the beam and the cracks in the PFR remain closed. As a result, torsional deformation behaviour does not display distinct cracked and un-cracked responses. Therefore, the torsion constant, *J*, for this particular set up can be assumed to be independent of the applied loading.

The rotation of the section can now be calculated using a one-dimensional analysis. For thin walled box beams, the determination of the torsion constant and rotations can be found in [14, 8]:

$$\phi = \frac{TL}{4\mathrm{A}^2 G}\oint\frac{ds}{t} = \frac{TL}{JG} \tag{22}$$

This results in the well known Saint Venant torsion constant formula:

$$J = \frac{4A^2}{\oint\frac{ds}{t}} \tag{23}$$

where: T is the applied torque, L is the length of the beam, G is the shear modulus of the beam, ϕ is the angle of rotation as shown on Figure 9, the integral in the denominator is taken along the centre line of the wall section (for example, the integral of an RHS with dimensions $D \times W$, web thickness t_w and flange thickness t_f equals:

$$\oint\frac{ds}{t} = 2\left(\frac{\left(D - t_f\right)}{t_w} + \frac{\left(W - t_w\right)}{t_f}\right) \tag{24}$$

and $$\mathrm{A} = \left(D - t_f\right)\left(W - t_w\right). \tag{25}$$

Through the use of the transformed section approach, the above formulas may be applied to determine the shear constant and deformations of the beam. Because of the geometry of the section, the transformation is carried out in a cylindrical coordinate system about the centre of rotation of the beam. A simplification is to set the transformed flanges to the y-axis transformation formula:

$$t_{ti} = t_i\frac{G_i}{G} \tag{26}$$

and the webs to the x-axis transformation formula as:

$$w_{ti} = w_i\frac{G_i}{G} \tag{27}$$

Where: t_{ti} is the transformed thickness, w_{ti} is the transformed width, G_i is the shear modulus, of laminate i, and G is the reference modulus of the transformed section. A justification of this approach is given in [15].

The resulting torsion constant can now be used within the model to estimate lateral torsional buckling behaviour.

Simplified analysis of lateral torsional buckling

The behaviour of an unrestrained beam under an increasing moment is illustrated on Figure 10. Minor imperfections in the beam and loading arrangement can result in the beam twisting slightly with increased loading. In region 1, as depicted on the graph, the behaviour of the beam is stable. However, as the end of region 1 is approached, the rotation of the section increases markedly. At this critical loading, the beam is no longer stable as it continues to twist without addition of further loading, which ultimately results in its failure.

Analytical formulation of lateral torsional buckling behaviour

Figure 11 represents the free end of the cantilever beam with an applied load, P. Due to the large displacements, the updated configuration, and the additional torque, $P\delta x$, are obtained iteratively.

The derivation of the iterative approach is detailed in [7] and results in expressions for the x-axis deflection, y-axis deflection and rotations respectively equalling:

$$\delta x = \frac{L^3 P}{3} \sin\left(\frac{P\delta x L}{4GJ}\right) \cos\left(\frac{P\delta x L}{4GJ}\right) \left[\frac{1}{EI_y} - \frac{1}{EI_x}\right] \tag{28}$$

$$\delta y = P\left[\left(\frac{L^3}{3EI_y}+\frac{L}{GA_s}\right)\sin^2\left(\frac{P\delta xL}{4GJ}\right)+\left(\frac{L^3}{3EI_x}+\frac{L}{GA_s}\right)\cos^2\left(\frac{P\delta xL}{4GJ}\right)\right] \quad (29)$$

and $$\phi = \frac{P\delta xL}{4GJ} \quad (30)$$

where L is the cantilever length, EI_x and EI_y are respectively the bending stiffness of the beam in the x and y directions, and δx, δy, and ϕ are shown on Figure 11.

Equations (28), (29) and (30) are solved for δx, δy, and ϕ. If the torsional resistance of the beam is greater than the average applied torque, $P\delta x/4$, the beam will not buckle and ϕ will converge to zero. The onset of buckling is observed if ϕ does not result in zero. The critical buckling moment is asymptotic to the resulting graph of P versus ϕ as shown on Figure 10.

Critical buckling moment formulas

The previously developed approach describes the load deformation path of the beam under torsional buckling. However, from a designer point of view only the critical buckling load is of interest. This can be obtained using equations based upon Euler buckling theory. A number of equations, for the critical buckling moment have been presented in design literature. Following is a discussion of a generalised approach, and the other one specifically developed for FRP beams.

Generalised approach

According to [12], the critical lateral torsional buckling moment of a steel beam is given as:

$$M_{cr} = \sqrt{\frac{\pi^2}{L^2}EI_yGJ + \frac{\pi^4}{L^4}EI_yEI_{warp}} \quad (31)$$

where: M_{cr} is the critical buckling moment, L is the length of the beam between lateral restraints, EI_y is the stiffness of the beam about the y-axis, GJ is the torsional stiffness of the beam, and EI_{warp} is the warping stiffness of the beam. For an RHS, I_{warp} is taken as zero as the section is doubly symmetric.

This formula is for the specific case of a simply supported beam subjected to pure moment loading. To allow for other loading and boundary conditions equation (31) is altered to:

$$M_{cr} = C_b \sqrt{\frac{\pi^2}{L_{ef}^2} EI_y GJ + \frac{\pi^4}{L_{ef}^4} EI_y EI_{warp}} \tag{32}$$

where the coefficient C_b is incorporated to allow for the loading arrangement on the beam and L_{ef} is the effective length of the beam, which is related to the end restraints. Gaylord et al. gives a range of 1.28 to 1.71 for C_b, and L_{ef} equalling L for the cantilever beam.

Specific approach for composite beam

The Eurocomp Design Code [10] presents a formula for lateral torsional buckling specifically for FRPs:

$$M_b = \frac{\sqrt[4]{\frac{\pi^6}{L_{ef}^6} E^3 I_y^3 GJ + \frac{K\pi^8}{L_{ef}^8} E^4 I_y^3 I_{warp}}}{C_1} \tag{33}$$

where: K = 0.5 for fully-fixed end condition, and C_1 is depending upon K, and the loading arrangement. For a cantilever with point load at its end K = 0.5 and C_1 = 1.0.

The factors given in [10] are only applicable to simply-supported doubly-symmetrical beams that are loaded through their shear centre. However, as shown on Figure 12, the use of the equation does not yield satisfactory results when compared against the analytical and the generalised approach.

KEY FINDINGS

From the bending and shear investigations it became apparent that the thicknesses of the flanges and webs greatly affect the performance of the beam. Indeed, providing adequate thickness to the flanges and webs could avert all the possible second-order failure modes. In addition, the core material is comparatively cheap compared to the laminates, and it does not have a key function as regards to the primary failure modes.

Altering the flange thickness does not have a significant effect upon shear capacity, as the webs provide the majority of the shear resistance of the beam. However, it does affect the moment resisting capacity of the beam. As shown on Figure 13, there is an optimum value for top flange core thickness. Below the optimum, the beam is susceptible to flange buckling and punching failures. Once the thickness rises above the optimum, beam capacity falls due to the rise in neutral axis and proportional rise in tensile strains in the bottom laminate.

Because of cracking, the thickness of the core material in the bottom flange is less influenced by a shift in the neutral axis. However, as shown on Figure 14, insufficient material results in a lower capacity of the beam due to the prevalence of bottom flange punching.

When web thickness is varied, as shown on Figure 15, both shear and moment capacities exhibit different responses. In both cases, primary failure occurs once the web thickness is over an optimal value.

CONCLUSIONS

The thin walled beam theory was used to investigate the behaviour of the beam under shear loading. It was found that the laminates constitute the main shear reinforcement of the beam, particularly those placed in the webs. However, if insufficient core material is provided within the webs and flanges, secondary failure modes such as buckling of the webs and punching shear of the flange could precede primary shear failure. The formulas presented in this part together with those developed in the preceding prequel for bending have been used to investigate the combined moment – shear loading. The combined model was found to replicate the known interaction between shear and bending.

Lateral instability is another reason for secondary failure of FRP beams. Using the transformed section, an iterative method describing the load deformation behaviour was developed. This approach has been also incorporated into two programs to respectively predict the torsional and lateral torsional buckling behaviour of the beam

REFERENCES

1. Bank LC. Shear coefficients for thin-walled composite beams. Composite Structures 1987; 8: 46-61.
2. Bank LC. Flexural and shear moduli of full-section fiber reinforced plastic (FRP) pultruded beams. Journal of Testing and Evaluation. 1989; 17(1): 40-45.

3. Barbero EJ, Fu SH, Raftoyiannis I. Ultimate bending strength of composite beams. Journal of Materials in Civil Engineering. 1991; 3(4):292-306.
4. Davalos JF, Salim P., Qiao R, Lopez-Anido R, Barbero, E J. Analysis and design of pultruded FRP shapes under bending. Composites Part B: Engineering, 1996; 27(3/4): 295-306.
5. Kilic O, Aktas A, Dirikolu MH. An investigation of the effects of shear on the deflection of an orthotropic cantilever beam by the use of anisotropic elasticity theory. Composites science and technology. 2001; 61(14): 2055-2061.
6. Nagaraj V, Gangarao HVS. Static Behavior of Pultruded GFRP Beams. Journal of Composites for Construction. 1997; 1(3):120-129
7. Springolo, M. New fibre-reinforced polymer box beam: investigation of static behaviour. PhD thesis. Faculty of Engineering, The University of Southern Queensland, Australia. 2005. http://adt.usq.edu.au/adt-QUSQ/public/adt-QUSQ20050421.122411/
8. Beer FP, Johnston ER. Mechanics of Materials. McGraw-Hill Ryerson Ltd, Singapore 1985.
9. Bulson PS., The Stability of Flat Plates. Chatto & Windus, London. 1970
10. Clarke JL. (ed.). Structural Design of Polymer Composites; Eurocomp Design Code. E & FN Spon, Chapman & Hall. 1996
11. Dym CL, Shames IH. Solid Mechanics, a variational approach. McGraw-Hill Kogakusha, Tokyo. 1973
12. Gaylord EH., Gaylord CN, Stallmeyer JE. Design of Steel Structures, 3Ed, McGraw-Hill, Singapore. 1992
13. Hibbeler RC. Mechanics of Materials, 1st Ed, Maxwell Macmillan International, New York. 1991

14. Heins CP. Bending and Torsional Design in Structural Members. Lexington Books, Lexington, Massachusetts. 1975
15. Kollbrunner CF, Basler K. Torsion in Structures: An Engineering Approach. Springer-Verlag, Berlin. 1969

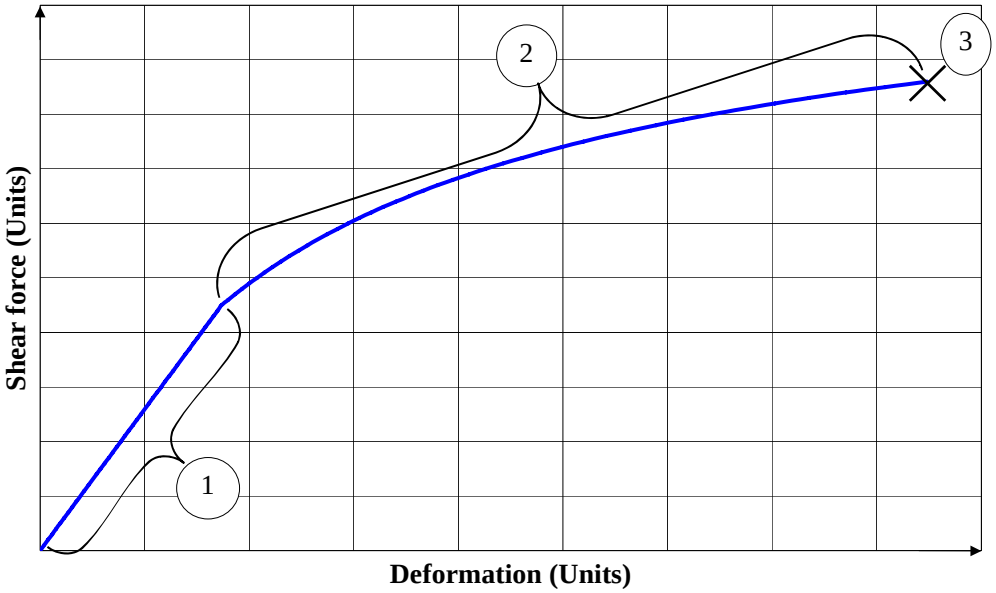

Figure1: FRP beam; shear load deformation behaviour

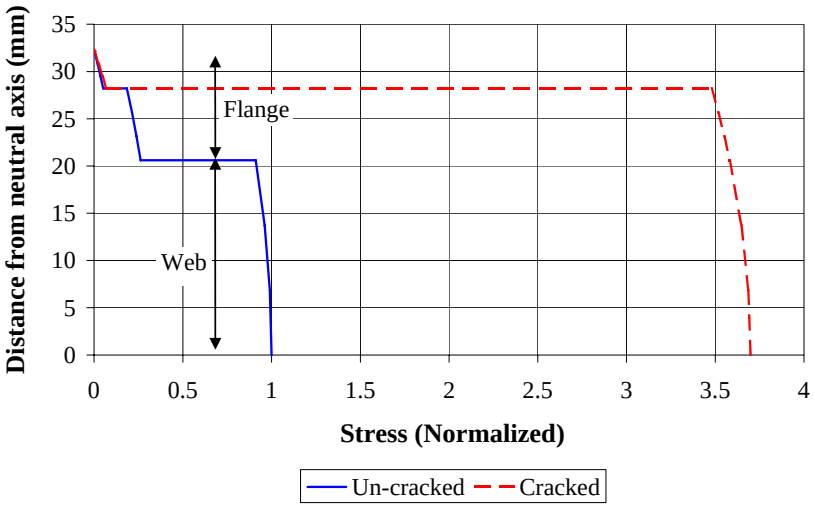

Figure 2: Shear stresses throughout the beam cross-section

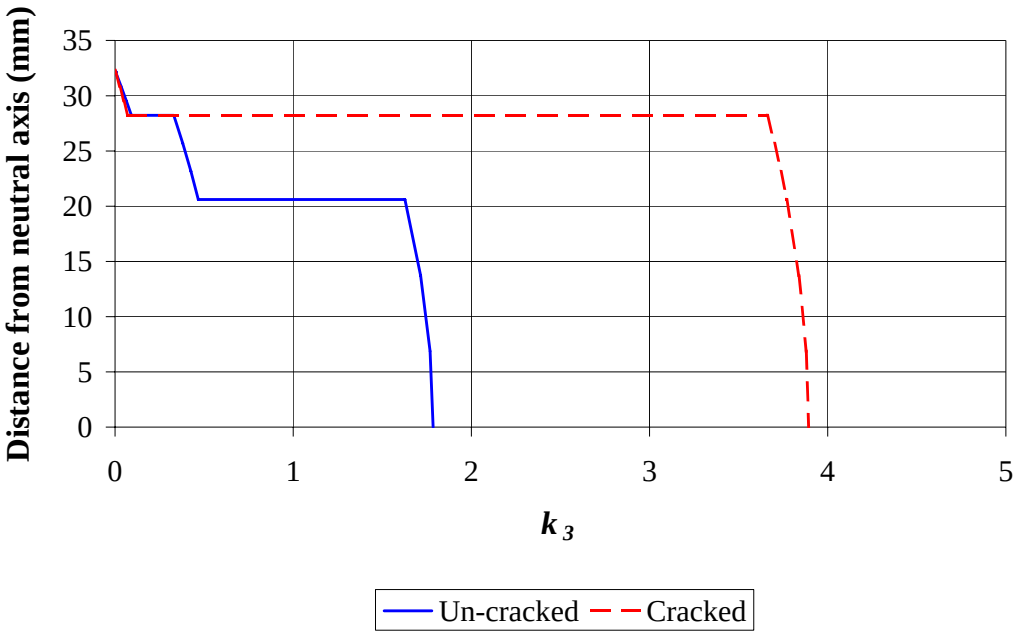

Figure 3: Shear correction values throughout the beam

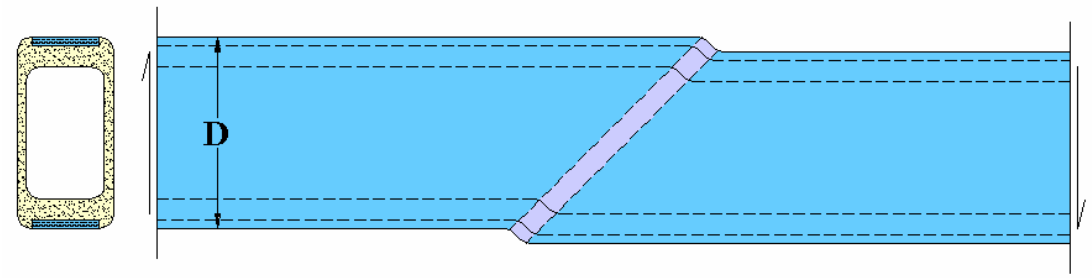

Figure 4: Localised shear dislocation caused by cracking of the PFR

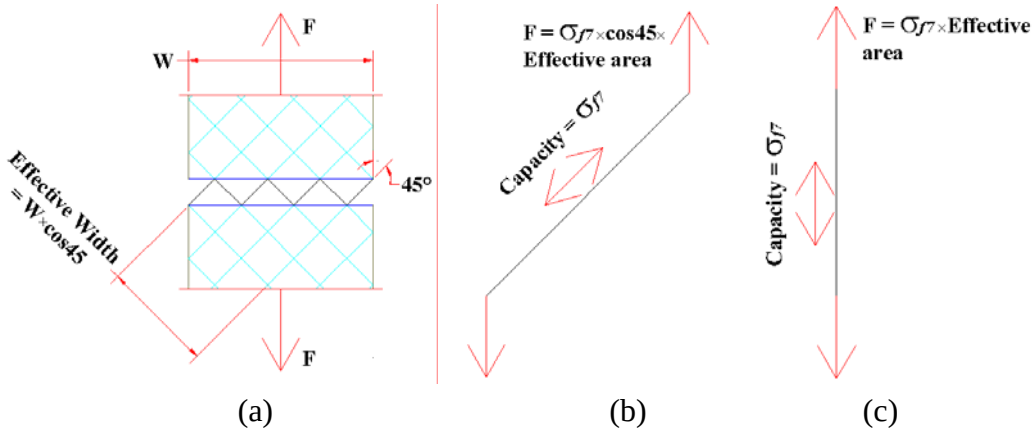

Figure 5**:** Free body diagrams of the initial and final fibre orientation at a crack

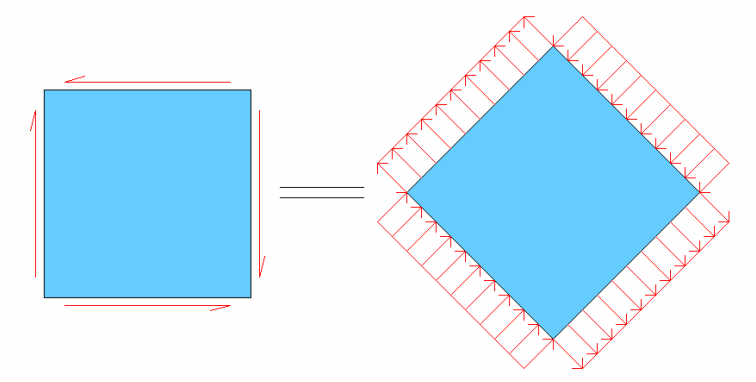

Figure 6: Principal stresses on the webs

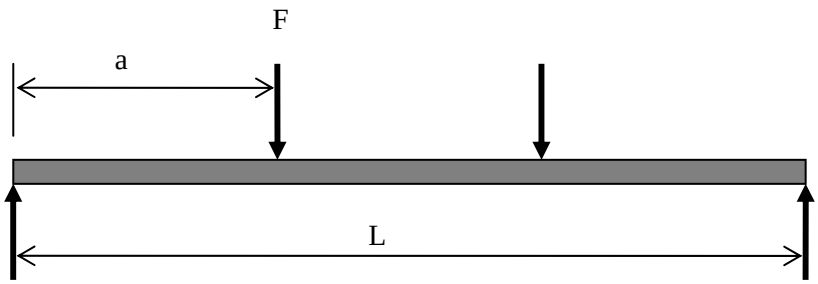

Figure 7: Beam in four-point bending

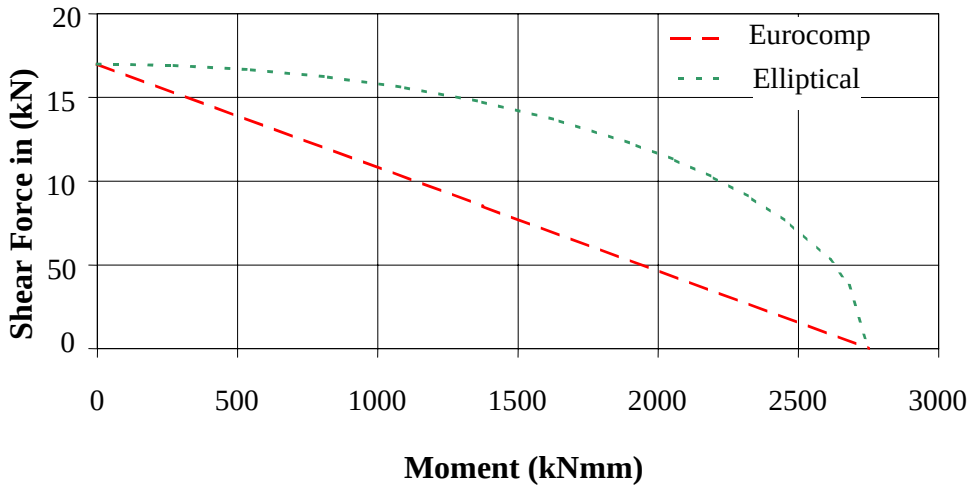

Figure 8: Moment-shear interaction diagrams

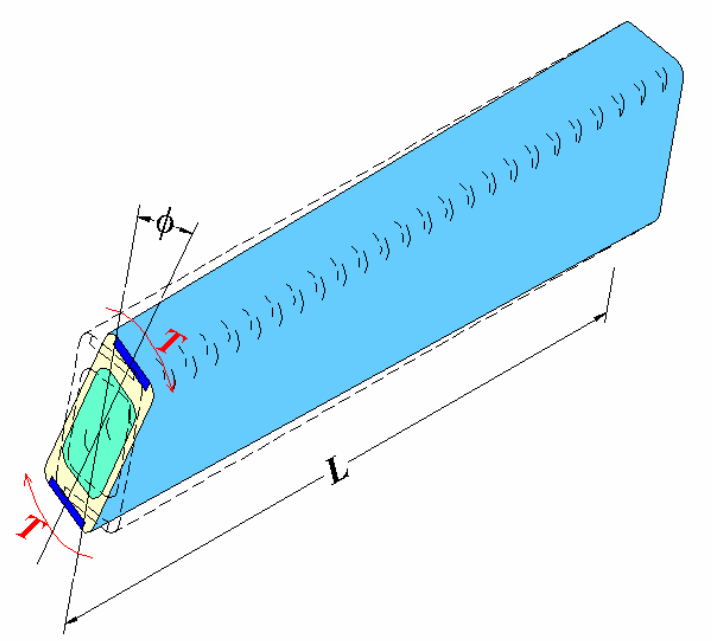

Figure 9: Torsional rotation of the Beam

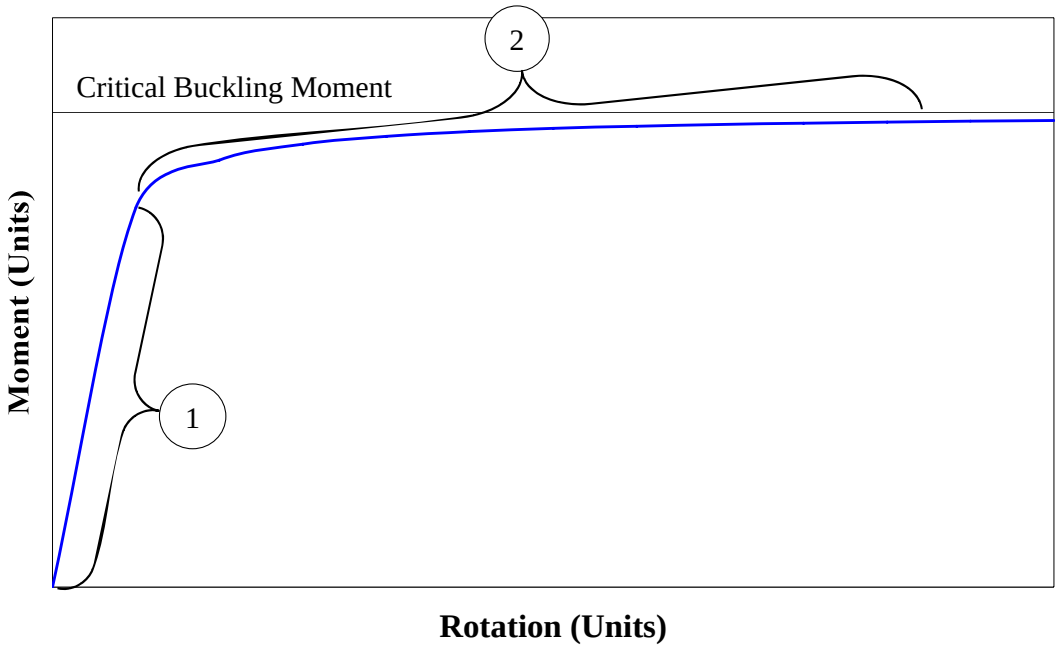

Figure 10: Lateral buckling behaviour of the FRP beam

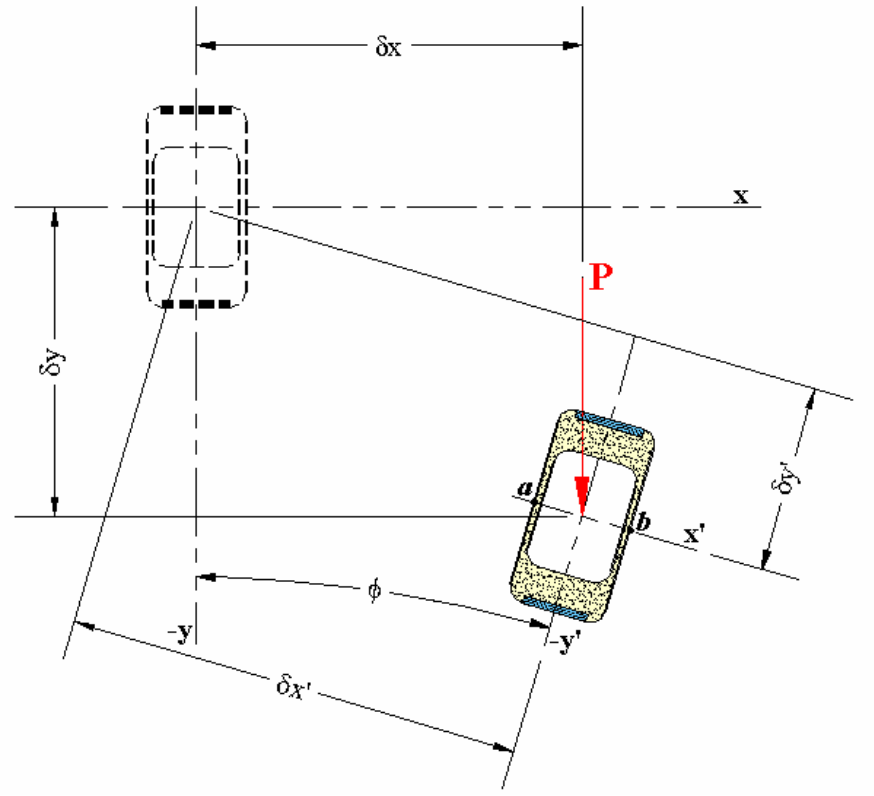

Figure 11: Deflections of a beam undergoing lateral torsional buckling

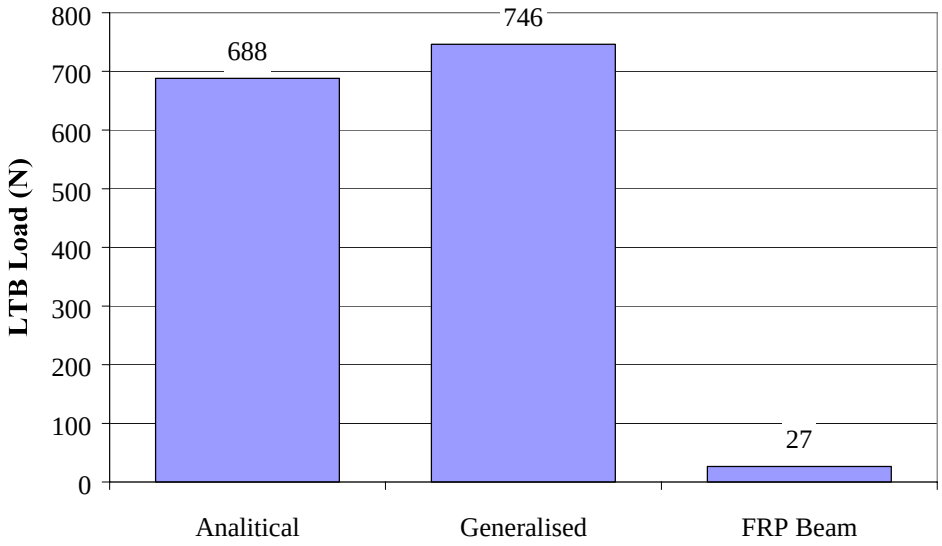

Figure 12: Comparison of methods to determine the critical buckling moment

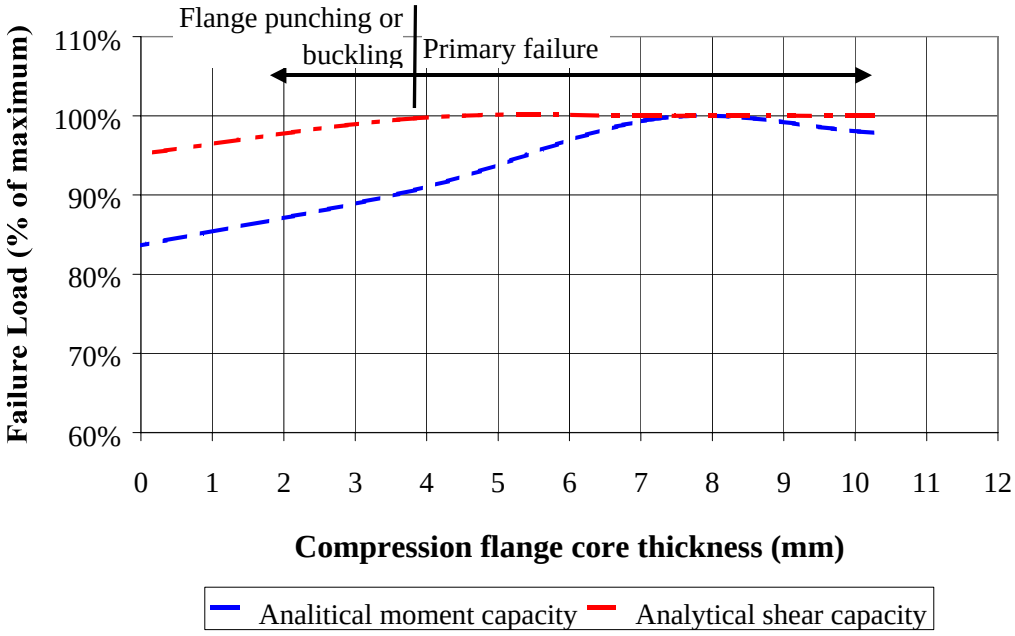

Figure 13: Effect on capacity by varying top flange core thickness

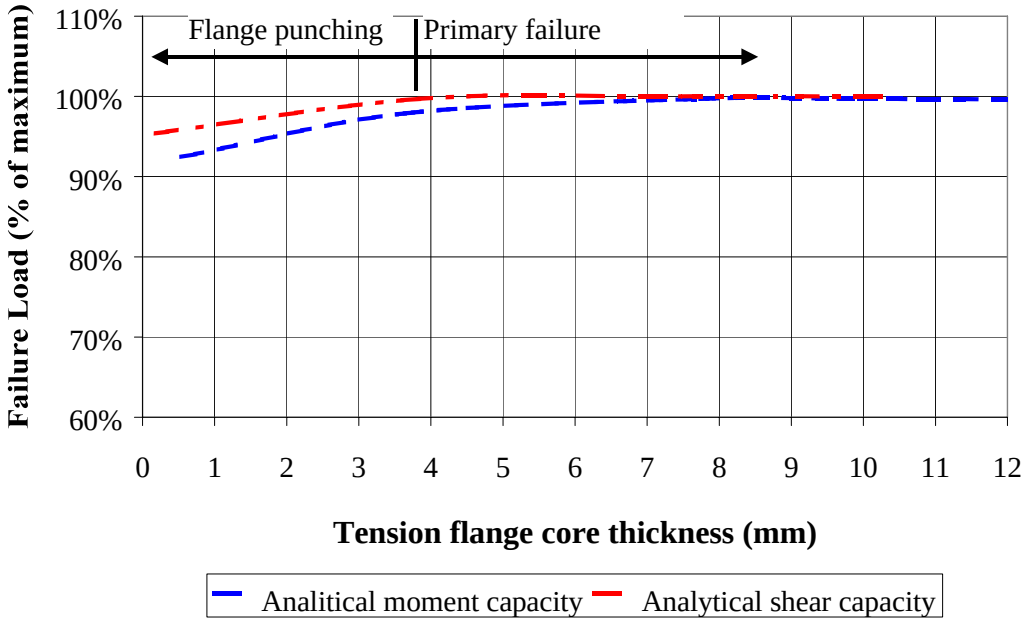

Figure 14: Effect on capacity by varying bottom flange core thickness

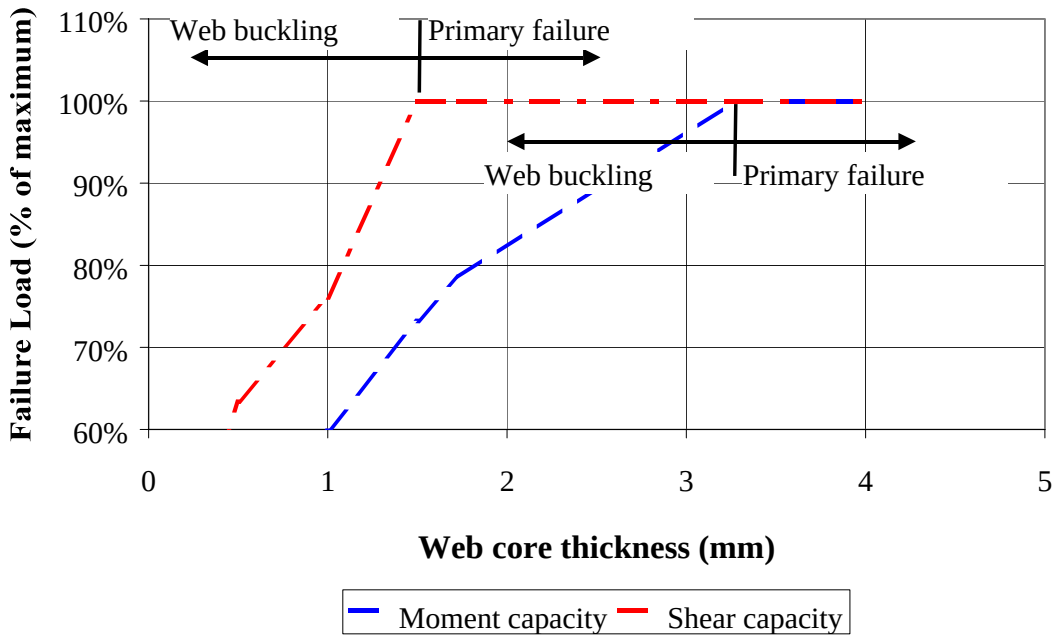

Figure 15: Effect on shear and moment capacities by varying web thickness